

# Ultrabroadband dielectric spectroscopy and phonons in $(\text{Pb}_{1-x/2}\text{La}_x)(\text{Zr}_{0.9}\text{Ti}_{0.1})\text{O}_3$

E. Buixaderas,<sup>1,a)</sup> V. Bovtun,<sup>1</sup> S. Veljko,<sup>1</sup> M. Savinov,<sup>1</sup> P. Kužel,<sup>1</sup> I. Gregora,<sup>1</sup> S. Kamba,<sup>1</sup> and I. Reaney<sup>2</sup>

<sup>1</sup>*Institute of Physics, ASCR, Na Slovance 2, 182 21 Prague 8, Czech Republic*

<sup>2</sup>*University of Sheffield, Mappin Street, Sheffield S1 3JD, United Kingdom*

(Received 13 August 2010; accepted 12 September 2010; published online 17 November 2010)

The dielectric behavior of  $(\text{Pb}_{1-x/2}\text{La}_x)(\text{Zr}_{0.9}\text{Ti}_{0.1})\text{O}_3$  PLZT 100x/90/10 ( $0 \leq 100x \leq 1$ ) was studied in the frequency range  $10^2$ – $10^{14}$  Hz using dielectric, time-domain terahertz (THz), far-infrared, and Raman spectroscopy in the temperature interval 10–900 K. PZT 90/10 and PLZT 2/90/10 undergo two phase transitions, from a cubic paraelectric to a rhombohedral untitled ferroelectric (FE) phase and on further cooling to a tilted FE phase. PLZT 4/90/10 and PLZT 10/90/10 are incommensurately modulated and composed of an intergrowth of polar and antipolar cation displacements. These samples consequently demonstrate a FE soft mode which exhibits minimal frequency several tens of degrees above the nominal antiferroelectric phase transition temperature. The dielectric response of PLZT 100x/90/10 is mainly governed by a gigahertz relaxation and a soft phonon component in the THz range. As in other PbO-based perovskites, the soft mode is split into a higher-frequency component ( $\omega \sim 80 \text{ cm}^{-1}$ ) and a highly damped THz component ( $\omega \sim 30 \text{ cm}^{-1}$ ), with larger dielectric strength already in the paraelectric phase. © 2010 American Institute of Physics. [doi:10.1063/1.3501105]

## I. INTRODUCTION

Lead lanthanum zirconate titanate ceramics  $(\text{Pb}_{1-x/2}\text{La}_x)(\text{Zr}_y\text{Ti}_{1-y})\text{O}_3$  [PLZT 100x/100y/100(1–y)] are known for their exceptional optical and dielectric properties which were initially discovered and reviewed by Land *et al.*<sup>1</sup> Doping of  $\text{Pb}(\text{Zr}_y\text{Ti}_{1-y})\text{O}_3$  (PZT) with La is known to induce considerable A-site disorder since La (replacing Pb) is compensated by  $1/2V'_{\text{pb}}$  vacancies. The presence of these two types of defects disrupts long range ferroelectric (FE) order and ultimately induces a relaxor state as the concentration of La increases. However, the relationship between the local structure and macroscopic properties is still a source of great controversy.

The first phase diagram of PLZT was established by Haertling.<sup>2</sup> The Ti-rich part of the diagram shows tetragonal symmetry (for zero La percentage content) and the Zr-rich part is macroscopically rhombohedral for Zr contents between 90% and 50% approximately.<sup>1,2</sup> Samples with the highest Zr concentration are antiferroelectric (AFE), a characteristic for the parent compound  $\text{PbZrO}_3$  which is orthorhombic with *Pbam* symmetry. Despite the phase diagram of Haertling,<sup>2</sup> the symmetry of the PLZT 100x/90/10 system in particular is still controversial. At room temperature, PZT 90/10 is FE and exhibits macroscopic rhombohedral symmetry (*R3c*) with a doubled unit cell.<sup>3</sup> However, superstructure peaks in the neutron<sup>4</sup> and electron diffraction<sup>5</sup> data suggest that either the local symmetry is lower (*Pc*) or that compositions are multiphase.<sup>4,6</sup> Pulsed neutron diffraction data<sup>7</sup> also supported that the local structure of PZT 90/10 at room temperature is more complicated than the tilted rhombohedral model.

PLZT with  $x \leq 0.02$  possess similar structure to undoped samples but for  $2 < 100x \leq 4$  there is a significant change in the polar character.<sup>5</sup> PLZT 4/90/10 appears macroscopically tetragonal by in-house x-ray diffraction (XRD) (Ref. 5) but the authors of Ref. 6 using a higher resolution XRD source refined PLZT 4/90/10 and PLZT 6/90/10 as orthorhombic instead of tetragonal. Coexistence of rhombohedral and orthorhombic symmetry was found also in Ref. 8. Early work by Jona *et al.*<sup>9</sup> on x-ray and neutron diffraction of PLZT commented that the peculiar relation between the orthorhombic axis, i.e.,  $b=2a$ , could give rise to an apparent tetragonal rather than orthorhombic structure if the superstructure reflections associated with antiparallel cation displacements were not apparent in the diffraction data or were ignored.

Electron diffraction data revealed that PLZT 4/90/10 has an incommensurate modulation along a  $\langle 110 \rangle$  direction.<sup>5,10</sup> The introduction of La in the lattice develops an intergrowth of FE and AFE states with similar energies. A slight change in composition turns the sample AFE or FE, and the competition between both leads to the incommensurate state.<sup>10–12</sup> Theoretical studies by Ishchuk<sup>13</sup> also relate the broad boundary between the FE and the AFE state in PLZT as due to these states. The incommensurate state is difficult to detect by in-house XRD and compositions do not exhibit discrete superstructure and appear macroscopically tetragonal, in accordance with the comments of Jona *et al.*<sup>9</sup> Very recently, it was found that PLZT 100x/90/10 show incommensurate regions even for very low La content. From the orientation of domains it was concluded that the structure of the incommensurate AFE regions in PLZT is very similar to that one of AFE  $\text{PbZrO}_3$ .<sup>14</sup>

A Raman soft mode of the E(TO) symmetry connected

<sup>a)</sup>Electronic mail: buixader@fzu.cz.

with the phase transition from the cubic paraelectric (PE) to the FE rhombohedral phase was found by Bauerle *et al.* in the FE phase of PZT 90/10 ceramics<sup>15</sup> and single crystals.<sup>16</sup> PLZT 2/92/8 ceramics were studied by x-ray and Raman scattering<sup>17</sup> which confirmed the coexistence of the rhombohedral FE phase with the orthorhombic AFE phase and corroborated the premise that a pressure-induced phase transition from a FE to an orthorhombic AFE phase in PZT 90/10 is feasible.<sup>18</sup> Some infrared (IR) data were published on PLZT 2/95/5 ceramics<sup>19,20</sup> and thin films,<sup>21</sup> where the soft mode was found below the Curie temperature  $T_C$  but IR spectra were mostly missing for this section of the phase diagram. In a recent contribution, the present authors discovered the presence of anomalous mode softening in PLZT 100x/90/10 ceramics using far-IR, Raman and time-domain terahertz (TDTHz) spectroscopies.<sup>22</sup> Samples with higher La content (4% and 10%) displayed nonclassical phonon softening described by  $\omega^2 = a(T - T_C)^\gamma$  with  $\gamma = 2/3$ . The current contribution presents dielectric spectroscopy ( $10^2$ – $10^9$  Hz) data and analyze them together with Raman, THz and IR results. The combination of these techniques reveals that the local structure of PLZT has symmetry lower than rhombohedral due to the higher number of IR and Raman modes but also show experimentally the coexistence of FE and AFE states with increasing La content in the behavior of the FE soft mode. This soft mode is split into two components and the dielectric response is also driven by a lower frequency excitation.

## II. EXPERIMENTAL TECHNIQUES

PLZT 100x/90/10 samples with 100x=2, 4, and 10 were prepared by a conventional mixed oxide synthesis using standard laboratory reagent grade powders (>99.9% purity). The density of all samples was greater than 95% of theoretical. XRD, transmission electron microscope, as well as some low-frequency dielectric measurements of these samples have been published previously.<sup>5</sup>

Dielectric experiments in the high-frequency range ( $10^6$ – $10^{10}$  Hz) were performed on cylindrically shaped samples of the following sizes:  $x=0$  and 0.02: D=0.4 mm, H=7.5 mm;  $x=0.04$ : D=0.5 mm, H=7.0 mm;  $x=0.1$ : D=0.65 mm, H=4.0 mm—where D is the diameter and H the height. A computer controlled high-frequency dielectric spectrometer equipped with AGILENT 4291B impedance analyzer, a Novocontrol BDS 2100 coaxial sample cell and a Sigma System M18 temperature chamber (operation range 100–570 K) were used in continuous frequency sweep measurements between 1 MHz and 1.8 GHz. Impedance spectra of the samples with Au electrodes sputtered on the bases of the cylinders were recorded on cooling with the rate of 1 K/min. The same rodlike samples were afterwards measured at 8.8 GHz using a TE<sub>0n1</sub> composite dielectric resonator.<sup>23</sup> Dielectric parameters of the measured samples were extracted by electrodynamic analysis of the resonator with and without the sample.

For low-frequency dielectric measurements ( $10^2$ – $10^6$  Hz) with a Hewlett-Packard 4192A impedance analyzer, gold electrodes were sputtered onto the faces of 1.8

mm thick plates. Samples were heated and cooled in the temperature range of 20–500 K with a rate of 3 K/min under a field of 2 V/cm.

IR reflectivity spectra were measured on polished ceramic disks (7 mm diameter and 1 mm thick) using a Fourier transform-IR spectrometer BRUKER IFS 113v. Room and high-temperature spectra were taken in the range 30–3000  $\text{cm}^{-1}$  with a resolution of 2  $\text{cm}^{-1}$  using two deuterated triglycine sulfate (DTGS) pyroelectric detectors. For high temperatures (300–900 K) a commercial oven SPECAC P/N 5850 was used. For low-temperature measurements (10–300 K) we used a continuous-flow Optistat CF (OXFORD INSTRUMENTS) cryostat with the sample mounted in a He gas bath. The use of polyethylene windows in cryostat reduced the accessible frequency range to 30–650  $\text{cm}^{-1}$  at low temperatures. Low-temperature spectra were detected by a He-cooled (1.6 K) Si bolometer.

TDTHz transmission measurements were carried out on thin polished plane-parallel samples (of 30  $\mu\text{m}$  thickness) in the temperature range of 20–900 K. A custom-made TDTHz transmission spectrometer was used to obtain the complex dielectric response of the samples in the THz spectral range. We used an experimental setup powered by a Ti:sapphire femtosecond laser oscillator described in detail in Ref. 24. Linearly polarized THz probing pulses were generated using an interdigitated photoconducting switch<sup>25</sup> and detected using the usual electro-optic sampling scheme with a 1 mm thick [110] ZnTe crystal.<sup>26</sup> The experiment provides the complex THz transmittance spectrum of the film:  $t(\omega) = E_s(\omega)/E_r(\omega)$  [where  $E_s(t)$  is the THz waveform transmitted through the investigated sample and  $E_r(t)$  the reference waveform obtained when the sample is removed from the THz beam path] from which the complex dielectric function was evaluated,<sup>24,27</sup> in the range 5–30  $\text{cm}^{-1}$  with a resolution of 0.5  $\text{cm}^{-1}$ ; at higher frequencies the samples were opaque. An Optistat CF cryostat with Mylar windows was used for measurements down to 20 K. Adapted commercial high-temperature cell SPECAC P/N 5850 was used to heat the samples up to 900 K.

Raman spectra were excited with the 514.5 nm line of an Ar laser at a power about 30 mW (~5 mW on the sample) and recorded in back-scattering geometry using a RM-1000 RENISHAW Raman microscope, equipped with a grating filter enabling good stray light rejection, in the 20–850  $\text{cm}^{-1}$  range. The diameter of the laser spot on the sample surface amounted to 2–3  $\mu\text{m}$ . A THMS-600 cell (LINKAM) was used for temperature control of the samples from 300 to 800 K. For low-temperature spectra (between 300 and 10 K) samples were loaded into a continuous-flow He cryostat (OXFORD INSTRUMENTS) and the microscope was equipped with a special angled arm carrying a  $\times 20$  ultra long working distance (ULWD) objective for efficient optical coupling. The spectral resolution was better than 2  $\text{cm}^{-1}$ .

## III. EXPERIMENTAL RESULTS

The experimental data set cover an ultrabroad spectral range from low ( $10^2$  Hz) up to the IR frequencies ( $10^{14}$  Hz). It is therefore impossible to fit all dielectric data

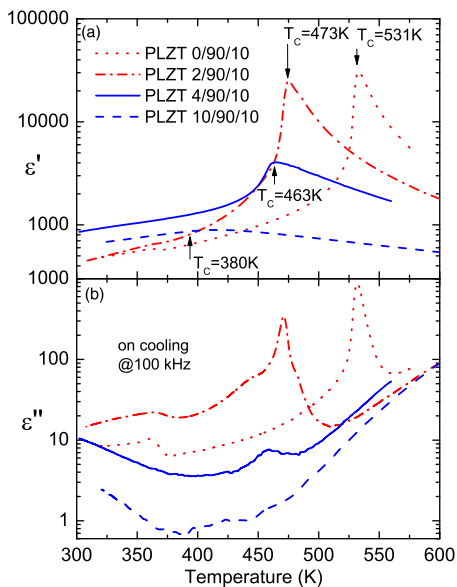


FIG. 1. (Color online) Permittivity (a) and dielectric loss (b) of PLZT 100x/90/10 ceramics at 100 kHz.

together using a single model. Then, the dielectric data is separated into two parts. The lower frequency data, including the gigahertz (GHz) and THz ranges, were fitted together to analyze the mutual influence of dielectric relaxations and the lowest frequency phonon mode. A generalized four-parameters oscillator model<sup>28</sup> was used for a common fit of THz and IR data which provides a better account for phonons.

### A. Dielectric results ( $10^2$ – $10^9$ Hz)

Results of the dielectric measurements obtained on cooling at 100 kHz are displayed in Fig. 1 for the four samples. Doping with lanthanum has a dramatic effect on the location and value of the permittivity maximum  $\epsilon'_{\max}$ . The sample without La shows a sharp  $\epsilon'(T)$  maximum at  $T_C=531$  K ( $\epsilon'_{\max} \sim 30\,000$ ). Substitution of Pb by La results in reduction of  $\epsilon'_{\max}$  and in the shift in the permittivity maximum to lower temperatures. For  $x=0.02$ ,  $T_C=473$  K ( $\epsilon'_{\max} \sim 25\,000$ ). These two samples are macroscopically rhombohedral according to XRD data<sup>5</sup> and on further cooling they show secondary maxima in the permittivity, resulting from a transition to a structure in which the unit cell is doubled by rotations of the oxygen octahedra. These two low-temperature phase transitions are more clearly seen in the loss spectra [Fig. 1(b)]. Samples with  $x>0.02$  display broader permittivity maxima and a strong reduction of the  $\epsilon'_{\max}$  values. For  $x=0.10$  a smeared maximum is displayed, with  $T_C \sim 380$  K and  $\epsilon' \sim 800$  [see Fig. 1(a)].

In Fig. 2, the inverse permittivity at 100 kHz is shown. Deviations from the Curie–Weiss behavior  $\epsilon' = C/(T - T_0)$ —where  $C$  is the Curie constant, and  $T_0$  is the Curie–Weiss temperature—are seen from the plot. Apart from the sample with  $x=0.10$ , all PLZT 100x/90/10 ceramics show first-order type phase transitions. For PLZT 10/90/10 the behavior of the inverse permittivity is different: disorder induced by La smears the phase transition, like in relaxor FEs. Parameters from the Curie–Weiss fits are presented in Table I. In

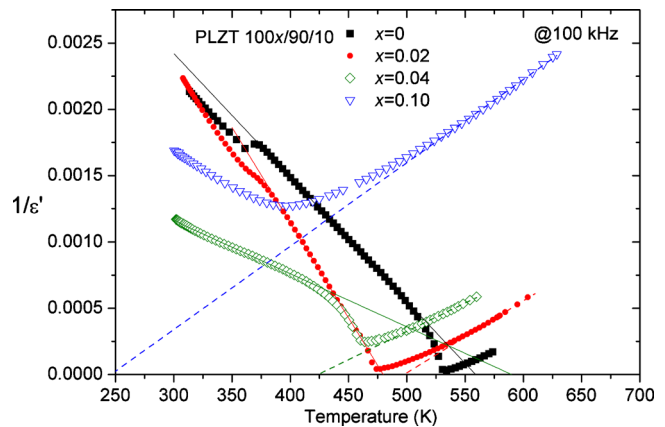


FIG. 2. (Color online) Inverse permittivity of PLZT 100x/90/10 ceramics at 100 kHz. Lines correspond to fits with Curie–Weiss law. Parameters are shown in Table I.

the PE phase, the temperature region where deviation appears ( $\Delta T$ ) increases with La content. For  $x=0$ , it was not possible to make a reliable fit in the PE phase, as the number of available data points were insufficient. The low-temperature phase transitions near 370 K (onset of cell doubling) in the samples  $x=0$  and 0.02 are apparent from the deviation of the Curie–Weiss fit from the experimental data in the FE phase.

Temperature dependence of the real and imaginary permittivity obtained at various frequencies is shown in Fig. 3. The  $\epsilon'$  values increase on lowering frequency, showing that relaxations below phonon frequencies are present in the dielectric response. Dielectric loss spectra  $\epsilon''$  show that a GHz relaxation plays a particularly important role near the phase transition. In order to understand better this behavior, the frequency dependences of the dielectric permittivity and loss for all the samples from  $10^4$  to  $10^{12}$  Hz (including the TDTHz data) are depicted in Fig. 4 for different temperatures together with their fits. The complex permittivity  $\epsilon^*(\nu)$  between the megahertz (MHz) and THz ranges was fitted by the sum of a Cole–Cole relaxation and a damped oscillator

$$\begin{aligned} \epsilon^*(\nu) &= \epsilon'(\nu) - i\epsilon''(\nu) \\ &= \frac{\Delta\epsilon_{\text{MW}}}{1 + (i\nu/\nu_{\text{MW}})^{1-\alpha}} + \frac{\Delta\epsilon_{\text{SM}}\nu_{\text{SM}}^2}{\nu_{\text{SM}}^2 - \nu^2 + i\gamma_{\text{SM}}\nu} + \epsilon_{\text{IR}}, \quad (1) \end{aligned}$$

where  $\Delta\epsilon_{\text{MW}}$  is the dielectric strength of the Cole–Cole re-

TABLE I. Parameters of the Curie–Weiss fit for PLZT 100x/90/10 ceramics.  $T_0^+$  and  $C^+$  are the fit parameters of  $1/\epsilon'$  approaching phase transition from above,  $T_C$  refers to the permittivity maximum,  $T_{\text{CW}}$  is the temperature above  $T_C$ , where deviations from the Curie–Weiss law start, and  $\Delta T$  is the temperature interval where the deviations are present.  $T_0^-$  and  $C^-$  are the fit parameters obtained from the data below  $T_C$ . All parameters given in degrees Kelvin.

100x (La %)	$T_0^+$	$C^+$	$T_C$	$T_{\text{CW}}$	$\Delta T$	$T_0^-$	$C^-$
0			531			559	106 966
2	498	184 072	473	564	66	480	69 678
4	423	233 823	463	503	80	586	244 729
10	246	159 054	380	530	284	615	187 408

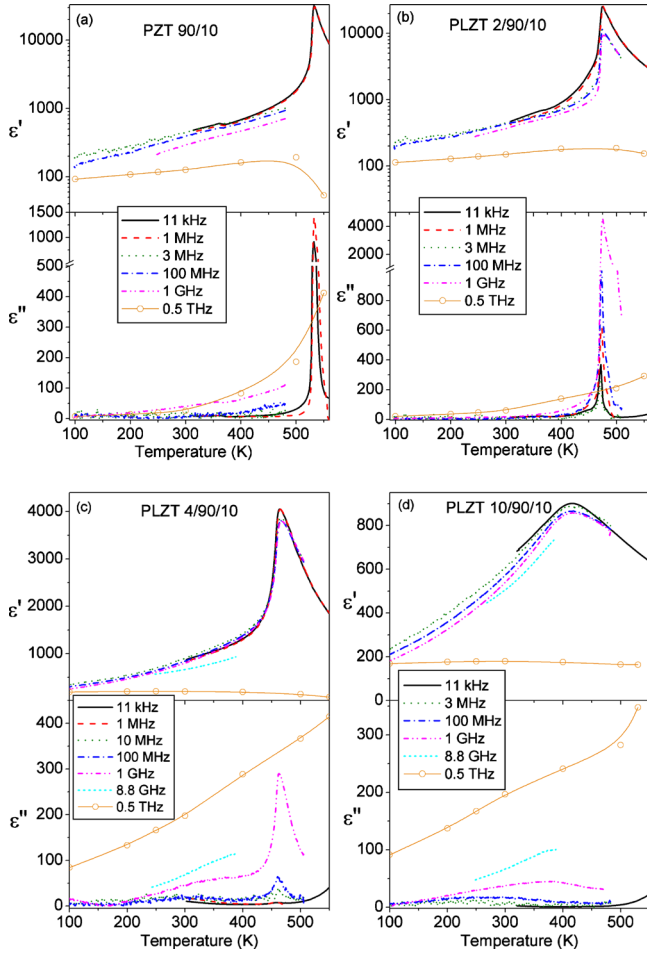


FIG. 3. (Color online) Dielectric permittivity  $\epsilon'(T)$  and loss  $\epsilon''(T)$  of PLZT 100 $x$ /90/ceramics at several frequencies. (a)  $x=0$ , (b)  $x=0.02$ , (c)  $x=0.04$ , (d)  $x=0.10$ .

laxation;  $\nu_{MW}$  its mean relaxation frequency,  $\alpha$  a real index between 0 and 1 which determines the deviation from the Debye model and characterizes the width of the distribution of the Debye relaxation frequencies;  $\Delta\epsilon_{SM}$ ,  $\nu_{SM}$ , and  $\gamma_{SM}$  denote the dielectric strength, frequency, and damping of the oscillator in the THz range, respectively; and  $\epsilon_{IR}$  is the dielectric contribution of phonons and electrons with frequencies higher than 2 THz. From Fig. 4, two excitations (corresponding to the two maxima in the dielectric loss spectra) are present between MHz and THz ranges. In the FE samples ( $x=0,0.02$ ) these excitations are well separated, but in samples for  $x=0.04$  and 0.10, where there is competition between FE and AFE behavior, their frequencies become closer to each other. The temperature dependence of the spectra indicates that at high temperatures (above  $T_C$ ) the two excitations merge into one.

## B. THz and IR results ( $10^{12}$ – $10^{14}$ Hz)

The measured IR reflectivity spectra were fitted together with the THz complex dielectric spectra obtained from the TDTHz experiment, using the factorized oscillator model of the dielectric function<sup>28</sup>

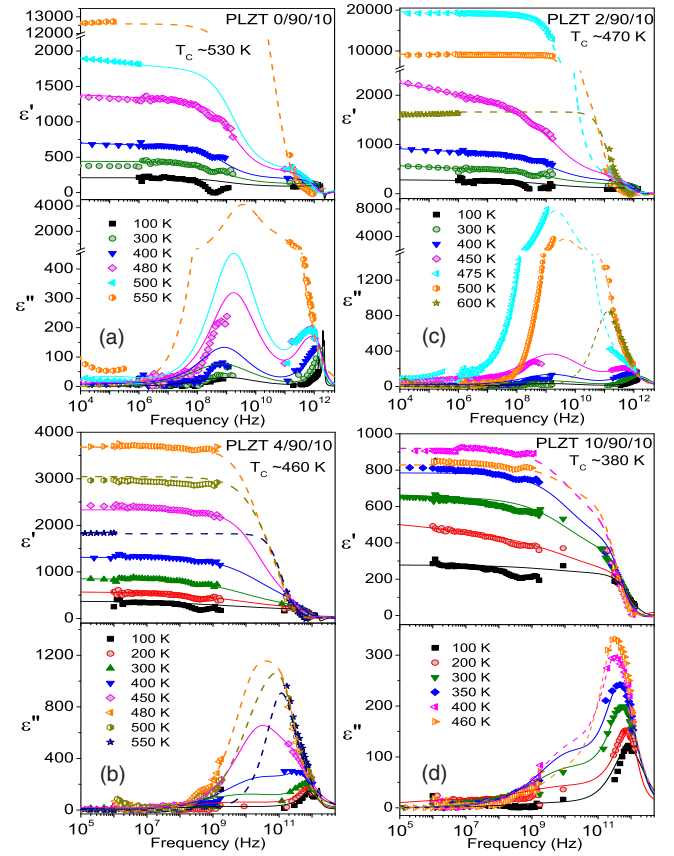


FIG. 4. (Color online) Frequency dependences of the dielectric permittivity  $\epsilon'(\nu)$  and loss  $\epsilon''(\nu)$  of PLZT 100 $x$ /90/10 ceramics at selected temperatures. (a)  $x=0$ , (b)  $x=0.02$ , (c)  $x=0.04$ , and (d)  $x=0.10$ . Symbols—experiment, lines—fits with Eq. (1). Note the break of the scale in (a) and (b) figures.

$$\epsilon^*(\nu) = \epsilon'(\nu) - i\epsilon''(\nu) = \epsilon_\infty \prod_{j=1}^n \frac{\nu_{LOj}^2 - \nu^2 + i\nu\gamma_{LOj}}{\nu_{TOj}^2 - \nu^2 + i\nu\gamma_{TOj}}, \quad (2a)$$

$$\Delta\epsilon_j = \frac{\epsilon_\infty}{\nu_{TOj}^2} \frac{\prod_k (\nu_{LOk}^2 - \nu_{TOj}^2)}{\prod_{k \neq j} (\nu_{TOk}^2 - \nu_{TOj}^2)}, \quad (2b)$$

where:  $\epsilon_\infty$  is the permittivity at frequencies much higher than all polar phonon frequencies;  $\nu_{TOj}$  and  $\nu_{LOj}$  are the transverse and longitudinal frequencies of the  $j$ th phonon mode;  $\gamma_{TOj}$  and  $\gamma_{LOj}$  the respective damping constants; and  $\Delta\epsilon_j$  refers to its dielectric contribution. The complex dielectric permittivity  $\epsilon^*(\nu)$  is related to the reflectivity spectrum  $R(\nu)$  by

$$R(\nu) = \left| \frac{\sqrt{\epsilon^*(\nu)} - 1}{\sqrt{\epsilon^*(\nu)} + 1} \right|^2. \quad (3)$$

The reflectivity spectra of PLZT 100 $x$ /90/10 at room temperature together with the corresponding fits using Eqs. (2) and (3) are shown in Fig. 5. Reflectivity points below  $30 \text{ cm}^{-1}$  were calculated from the TDTHz data and added to the reflectivity IR spectra, then, IR reflectivity,  $\epsilon'$  and  $\epsilon''$  were fitted simultaneously. Spectra above  $100 \text{ cm}^{-1}$  look very similar for all the samples, but there is an evident change in the phonon behavior in the low-frequency part, reflecting the change in symmetry on adding La. These phonons develop from the Last mode (i.e., the vibrations of

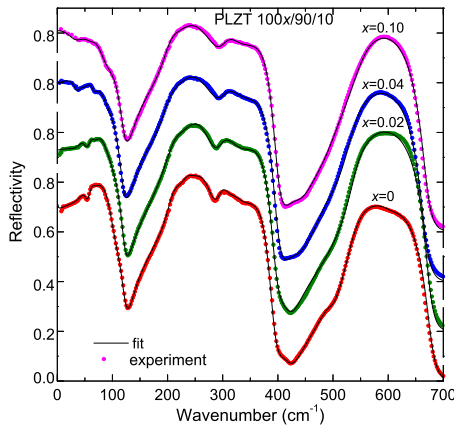


FIG. 5. (Color online) IR reflectivity spectra of PLZT 100x/90/10 ceramics at room temperature. Points—experiment, lines—fits with Eq. (2).

Pb and La cations against the oxygen octahedra), which has the lowest frequency from the 3  $F_{1u}$  cubic triplets in the  $Pm\bar{3}m$  cubic phase.

In Fig. 6, the temperature evolution of the reflectivity spectra for  $x=0.02$  and  $0.04$  is presented. In the cubic phase, both compositions show three main reflectivity bands with some substructure typical for cubic perovskites.<sup>29</sup> On cooling, their low-temperature phases show different phonon spectra, confirming the symmetry change between  $x=0.02$  and  $0.04$ . Phonons developing from the Last mode reveal different oscillator strengths of the Pb vibrations in these two compositions. In Tables II and III the phonon parameters obtained from the fits of the IR spectra at 300 and 20 K are shown. At the lowest temperature we fit 22 modes in  $x=0.02$  and 18 modes in  $x=0.04$ . The main difference between the samples is seen in phonons below  $100\text{ cm}^{-1}$ . At 20 K, the first mode in PLZT 4/90/10 has lower frequency and

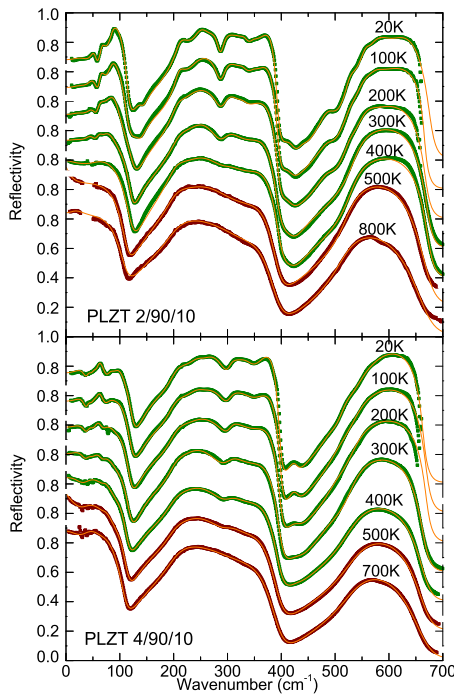


FIG. 6. (Color online) IR reflectivity spectra at different temperatures for PLZT 2/90/10 and PLZT 4/90/10.

TABLE II. Parameters of the IR transverse modes and Raman frequencies of PLZT 2/90/10 at 20 and 300 K.  $\nu_{\text{Ram}}$ ,  $\nu_{\text{TO}}$ , and  $\gamma_{\text{TO}}$  given in  $\text{cm}^{-1}$ . Italics refer to soft mode parameters. Tentative assignment of symmetries according to Ref. 30.

Symbol	PLZT 2/90/10							
	20 K				300 K			
	$\nu_{\text{Ram}}$	$\nu_{\text{TO}}$	$\gamma_{\text{TO}}$	$\Delta\epsilon$	$\nu_{\text{Ram}}$	$\nu_{\text{TO}}$	$\gamma_{\text{TO}}$	$\Delta\epsilon$
ETO1 <sub>CM</sub>	27							
	40	38.0	40.0	40.5	34	29.7	41.2	86.8
AFD	55	52.1	11.4	9.7	54	46.7	22.4	25.5
	71	66.4	7.8	10.8		61.4	17.0	17.8
ETO1' <sub>SM</sub>	82	77.1	12.9	11.2	70	71.4	19.7	9.0
	87	86.8	9.5	2.1				
		97.7	16.7	1.1		112.6	47.0	1.5
ELO1	121							
A <sub>1</sub> TO1	141	141.4	14.2	0.26		...		
A <sub>1</sub> TO1'	158					140		
A <sub>1</sub> LO1	182							
	196							
ETO2	212	208.5	14.1	7.8	209	208.3	27.6	11.1
ETO2'	247	243.2	30.4	3.0	235	237.5	55.4	1.3
	267	268.7	43.6	1.5		...		
ETO4	290	290.4	16.4	0.66	275	295.7	35.0	0.18
	311	314.5	27.7	0.02		...		
	330	325.5	29.1	0.25				
A <sub>1</sub> TO2	345	342.9	26.0	0.15		...		
A <sub>1</sub> TO2'		355.4	49.8	0.36	337	349.9	97.9	0.95
ELO2	403							
GR		413.5	53.2	0.17		421.3	47.8	0.02
A <sub>1</sub> LO2	421					415		
		437.1	30.9	0.08				
	447					...		
ETO3	494	485.2	31.8	0.34	490	...		
	512					...		
ETO3	528	525.6	19.3	0.30				
A <sub>1</sub> TO3	551	549.8	30.0	0.79	542	538.8	26.5	1.8
A <sub>1</sub> TO3'	569	563.2	21.6	0.05		578.1	76.8	0.2
		610.3	61.9	0.04				
ELO3/Ox. breath	677					677		
A <sub>1</sub> LO3	723					728		
Ox. breath	797					813		

this one and the mode at  $\sim 52\text{ cm}^{-1}$  show higher dielectric strength, almost twice, than the corresponding modes in PLZT 2/90/10. Contrarily, modes between 70 and  $100\text{ cm}^{-1}$  are more intense in PLZT 2/90/10. In addition, PLZT 4/90/10 shows a new mode near  $40\text{ cm}^{-1}$  absent in PLZT 2/90/10.

The experimental dielectric permittivity and loss in the THz range together with the calculated ones from the THz and far-IR fits [Eqs. (2) and (3)] are depicted in Fig. 7 for PLZT 2/90/10 and 4/90/10. An excitation seen in the THz spectra dramatically changes its frequency with temperature. The intensity of the loss peak below  $30\text{ cm}^{-1}$  increases on cooling, having a maximum at the PE-FE phase transition, and then it decreases. The frequency of the maximum also shifts to lower frequencies toward  $T_C$  and hardens on further cooling. The origin of this heavily damped excitation will be discussed below.

TABLE III. Parameters of the IR transverse modes and Raman frequencies of PLZT 4/90/10 at 20 and 300 K.  $\nu_{\text{Ram}}$ ,  $\nu_{\text{TO}}$ , and  $\gamma_{\text{TO}}$  given in  $\text{cm}^{-1}$ . Italics refer to soft mode component parameters.

PLZT 4/90/10								
Symbol	20 K				300 K			
	$\nu_{\text{Ram}}$	$\nu_{\text{TO}}$	$\gamma_{\text{TO}}$	$\Delta\varepsilon$	$\nu_{\text{Ram}}$	$\nu_{\text{TO}}$	$\gamma_{\text{TO}}$	$\Delta\varepsilon$
FE <sub>CM</sub>	25							
	37	32.2	27.9	87.5	32	26.8	34.8	236
		42.9	12.3	27.4	44	40.8	17.3	35.8
	49	51.5	14.7	28.9	53	55.8	22.0	20.4
FE <sub>SM</sub>	60	60.5	9.3	10.3				
	76	80.4	16.4	4.5	67	70.3	19.9	6.7
AFE <sub>SM</sub>		95.2	21.3	2.3		100.5	52.0	3.9
	117				98			
	147				127			
	189	174.9	69.4	7.1	170	174.9	79.4	7.5
	208	203.1	27.8	7.0	201	202.7	30.7	7.4
		238.5	45.1	0.53				
	261	260.3	37.8	0.59	248	230.4	65.5	0.48
	302	303.1	19.8	0.04	282	302.9	40.7	0.01
	326	330.2	62.6	0.43	339	349.5	109.3	0.83
	343	...						
	358	354.1	54.8	0.42				
	403							
	426	423.0	26.3	0.08		431.9	50.7	0.07
	471	493.3	31.4	0.15	478	490.2	50.1	0.16
	505	517.0	31.9	0.60	541	531.1	42.3	1.5
	545	540.8	50.3	0.80				
	568	575.4	78.3	0.01				
Ox. breath	703							
	734				724			
Ox. breath	776				800			

### C. Raman results

Raman scattering spectra of PLZT 2/90/10 and 4/90/10 –corrected for the Bose–Einstein factor— at several temperatures are depicted in Fig. 8. Both PLZT samples show similar weak bands in the cubic phase, although no first-order Raman activity is allowed in the  $Pm\bar{3}m$  structure. The origin of the observed Raman peaks was already discussed for PLZT 100x/40/60 (Ref. 30) and it was related to off-centering of cations. All Raman spectra were fitted with damped oscillators and their frequencies (and a tentative assignment of the symmetries of some modes for  $x=0.02$ ) are presented also in Tables II and III.

The main differences between the samples appear especially in the low-frequency part, below  $200 \text{ cm}^{-1}$ . On cooling, the strongest phonon in PLZT 2/90/10 hardens from  $\sim 60$  to  $80 \text{ cm}^{-1}$  and splits. New peaks develop and those are better viewed at the lowest temperature (20 K), where 30 modes were fitted. A small peak at  $680 \text{ cm}^{-1}$  appear at 300 K, which might be connected with the localized breathing mode of the oxygen octahedra when Zr content is high enough.<sup>31</sup>

The Raman spectra of PLZT 4/90/10, which is incompletely modulated also develops new features on cooling, however the total number of modes is lower (see Table III). No trace of the peak at  $680 \text{ cm}^{-1}$  is seen. In this sample

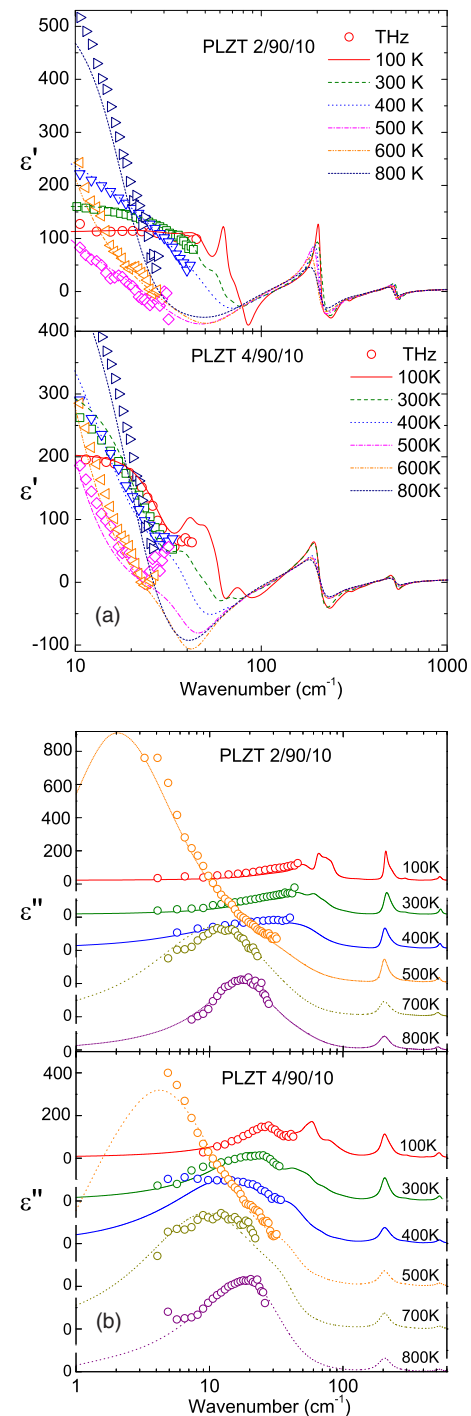


FIG. 7. (Color online) Permittivity (a) and dielectric loss (b) obtained from the fit to the reflectivity for PLZT 2/90/10 and PLZT 4/90/10 together with experimental points from the TDTHz experiment.

the strongest mode, which also hardens on cooling below  $T_C$  is located at higher wave numbers ( $\sim 70$  to  $120 \text{ cm}^{-1}$ ) than in the previous sample. An enhancement of the Raman signal below  $100 \text{ cm}^{-1}$  is seen at low temperatures in contrast to PLZT 2/90/10.

In Fig. 9 the temperature dependences of the IR and Raman mode frequencies are depicted for both mentioned samples. The main difference concerns the temperature behavior of the lowest frequency Raman mode. This mode softens on cooling toward  $T_C$  in PLZT 4/90/10 but toward the

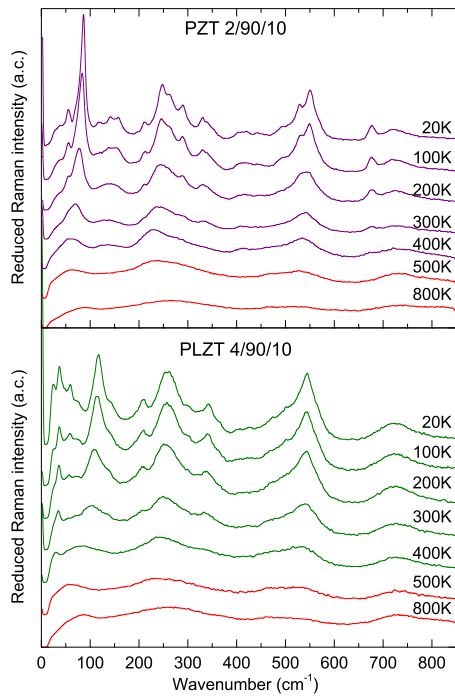


FIG. 8. (Color online) Raman spectra at different temperatures of PLZT 2/90/10 and PLZT 4/90/10.

secondary phase transition with unit cell doubling in PLZT 2/90/10. In the PE cubic phase, Raman modes activated by dynamic disorder of cations show different frequencies than the  $F_{1u}$  IR active modes. This is due to the different mode activities (first order Raman is forbidden) but also because the time scale of the Raman experiment is very short in comparison with the relaxation time of the dynamic disorder (hopping of atoms among available sites). In the FE phase IR frequencies agree rather well with those from Raman.  $E(TO)$  and  $A_1(TO)$  modes are simultaneously IR and Raman active, however, Raman spectra shows additional modes: longitudinal components and several modes above  $600\text{ cm}^{-1}$ , where

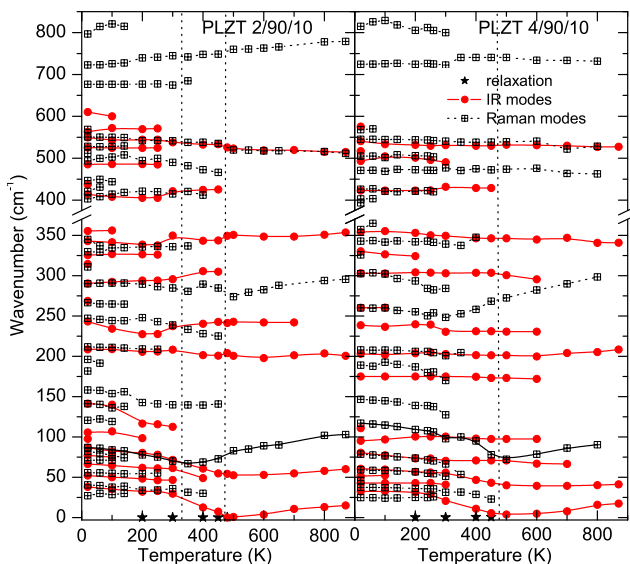


FIG. 9. (Color online) Temperature dependences of the Raman and IR transverse frequencies for PLZT 2/90/10 and PLZT 4/90/10. Vertical lines mark the critical phase transition temperatures.

nonpolar breathing modes of the oxygen octahedra are present. We should notice that, due to the dispersion in the  $k$ -vector in ceramics, the Raman frequencies are not pure TO or LO components but something in between.<sup>32</sup>

PLZT 2/90/10 shows two clear IR active soft modes not much affected by the second phase transition. These modes correspond to the two components of the FE soft mode, present in lead perovskites<sup>29</sup> and are coupled. The Raman active soft mode shows higher-frequency in the cubic phase and softens to the second phase transition, therefore, it must be coupled with a zone boundary mode.

In PLZT 4/90/10 there are also two IR modes which soften in a weaker manner, and a Raman soft mode related to  $T_C$  at higher frequencies, present also in the FE phase.

#### IV. DISCUSSION

Factor group analysis for PLZT with rhombohedral symmetry predicts  $3A_1(\text{IR,R})+4E(\text{IR,R})+1A_2(-)$  optical modes in the high-temperature FE phase (space group  $R3m$ ), and  $4A_1(\text{IR,R})+9E(\text{IR,R})+5A_2(-)$  modes in the low-temperature phase ( $R3c$ , with doubled unit cell).<sup>33</sup> This analysis considers long range ordered structures, without short-range correlated cation displacements such as described in Ref. 5 that reduce the local symmetry. Therefore, it is not surprising that IR and Raman experiments detect more modes than predicted from the factor group analysis utilizing these space groups. Multisite disorder of the Pb atoms was already experimentally discovered in the cubic phase of PZT by high energy synchrotron-radiation powder diffraction.<sup>34</sup> A similar disordered model was tested in the low-temperature phases to simulate satisfactorily the diffuse scattering in electron diffraction experiments.<sup>35</sup> Our IR results for  $x=0.02$ , which is still rhombohedral in average, agree with this disorder: 20 IR modes were found at 20 K, instead of 13 predicted. Some extra low-frequency modes could be accounted by disordered Pb, as in tetragonal PLZT.<sup>30</sup>

However, another symmetries were also proposed for PLZT  $100x/90/10$ . The  $Cc$  monoclinic symmetry group proposed by Knudsen *et al.*<sup>5</sup> would allow  $13 A'(\text{IR,R})+14A''(\text{IR,R})$  optic phonons. This means 27 simultaneously IR and Raman active modes in the low-temperature spectra. According to Breval *et al.*<sup>6</sup>  $x=0.02$  and  $0.04$  samples have orthorhombic symmetry ( $Pbam$  and  $C2mm$  groups respectively) at room temperature and lower temperatures. Comparing to  $\text{PbZrO}_3$  ( $Z=8$ ) 45 IR and 60 Raman modes could be expected. Our IR and Raman results at 20 K revealed at least 20 IR and 29 (TO and LO) Raman modes in PLZT 2/90/10 and 16 IR and 23 (TO and LO) Raman modes in PLZT 4/90/10. Consequently, these spectroscopic results could be explained by either a disordered rhombohedral phase, either a monoclinic group or an orthorhombic one. In any case these rather simple calculations support the premise that the local symmetry in PZT and PLZT near the AFE phase boundary is lower than currently described in the accepted phase diagrams.

The order parameter for the first FE phase transition is three dimensional and has  $F_{1u}$  symmetry in the PE phase. La

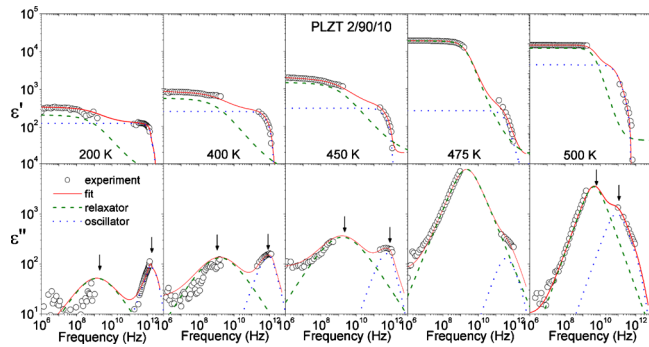


FIG. 10. (Color online) Frequency dependence of the complex permittivity of PLZT 2/90/10 at selected temperatures. Points: MHz and THz dielectric data, solid lines: fits with Eq. (1), and dashed lines: individual contributions of the GHz and THz excitations, respectively. Arrows denote maxima of  $\epsilon''$  at  $\nu_{\text{MW}}$  and  $\nu_{\text{SM}}$ .

substitution induces a modulated AFE phase at room temperature. If the nominal AFE phase transition is of the first-order type, as suggested by the inverse permittivity plots (Fig. 3), it should be driven by several lattice instabilities.<sup>36</sup> In pure  $\text{PbZrO}_3$ , the FE soft mode at  $\Gamma$ -point of the Brillouin zone (BZ) has a tendency to induce the FE phase transition. However, the FE phase does not develop due to stronger instabilities of two modes at the BZ boundary, which give rise to AFE order: the  $\Gamma_{25}$  mode at  $q=(1/2, 1/2, 1/2)$ , R-point, which tilts the O octahedra around the  $\langle 001 \rangle$  ( $\langle 011 \rangle$  in pseudocubic setting) axis, and the  $\Sigma_3$  mode with  $q=(1/4, 1/4, 0)$ , which produces antipolar displacements of Pb. Both modes drive the AFE phase transition and produce the unit cell multiplication.<sup>37,38</sup> In PLZT  $100x/90/10$ , there is similar behavior and several lattice instabilities appear at and out of the BZ center. This may trigger two different phase transitions where low-temperature phases have similar free energies. For  $x \leq 0.02$ , the free energy is minimal in the FE phase, although the AFE instabilities are also present. The  $M_3$  mode with  $q=(1/2, 1/2, 0)$  tilts the O octahedra around  $\langle 001 \rangle$  axis and induces a local tetragonal/orthorhombic symmetry<sup>9</sup> within the rhombohedral FE state.<sup>11</sup> This competition is likely to be the origin for the local reduction in symmetry described by the authors of Ref. 5 in these phase boundary compositions. For  $x > 0.02$ , the AFE phase has lower free energy and can develop into a mesoscopic or even macroscopic scale.

Broadband dielectric spectroscopy evidences two main excitations contributing to the dielectric response in all studied PLZT  $100x/90/10$  ceramics: one located in the GHz range and a second one in the THz range. A third one, below 1 MHz, was not taken into account because in some cases it is very broad and extends far below our measured range, so its full characterization was not possible. In Figs. 10 and 11, the frequency dependence of the complex permittivity for the FE PLZT 2/90/10 and the modulated AFE PLZT 4/90/10 is presented at various temperatures. The two excitations are clearly distinguished. At high temperatures their frequencies lie nearby and they merge into one asymmetric peak in the dielectric loss. On cooling two peaks develop. For PLZT 2/90/10 the contribution of the GHz relaxation to  $\epsilon''$  is about one order of magnitude higher around the phase transition.

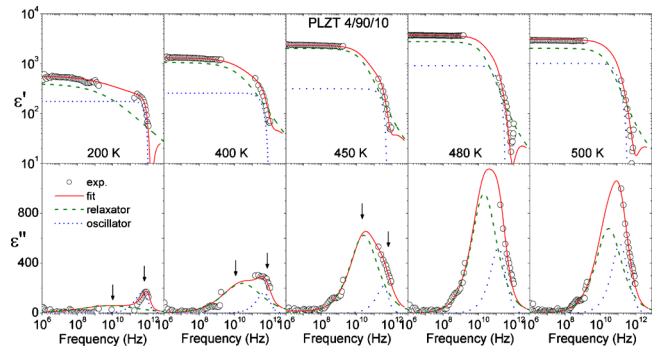


FIG. 11. (Color online) Frequency dependence of the complex permittivity of PLZT 4/90/10 at selected temperatures. Points: MHz and THz dielectric data, solid lines: fits with Eq. (1), and dashed lines: individual contributions of the GHz and THz excitations, respectively. Arrows denote maxima of  $\epsilon''$  at  $\nu_{\text{MW}}$  and  $\nu_{\text{SM}}$ .

This makes the permittivity near  $T_C$  higher for this sample. The GHz relaxation is a common feature of all FE ceramics. It is not related with the nature of the ferroelectricity but with domain walls and grain boundaries, although the microscopic mechanism is still under study.<sup>39,40</sup>

The temperature dependence of their frequencies  $\nu_{\text{MW}}$  and  $\nu_{\text{SM}}$  is shown in Fig. 12 for all the samples, together with frequencies calculated from the Raman and IR experiments. The frequency of the THz excitation fitted together with the low-frequency dielectric data corresponds very well to the lowest frequency IR or Raman phonon, and it is highly damped (see Table II). It displays softening toward  $T_C$  in all cases. These soft modes were identified as the FE soft modes, following the law  $\nu^2 = a(T - T_C)^\gamma$ . Nonclassical softening toward  $T_C$  was obtained (as in the IR fit) for the AFE samples when we allowed  $\gamma$  to change from 1 to 2/3.<sup>22</sup> In order to explain this behavior a new fit was carried out allowing the transition temperature to change. The fit (solid lines in Fig. 12) revealed that for  $x=0.04$  and 0.1, a classical softening ( $\gamma=1$ ) is allowed toward a temperature higher than  $T_C$  obtained from dielectric measurements—toward 489 K ( $T_C=463$  K) and 451 K ( $T_C=380$  K), respectively. The po-

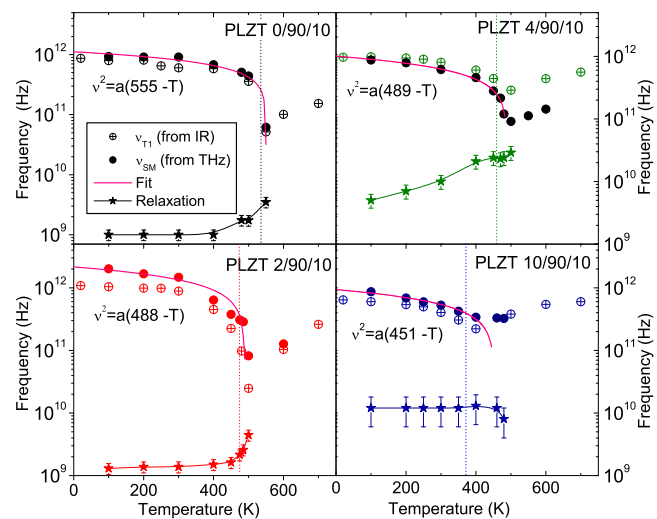


FIG. 12. (Color online) Temperature dependences of the frequencies of the soft mode and GHz relaxation in PLZT  $100x/90/10$ .

lar soft mode minimum above  $T_C$  seems to be connected with a local FE phase transition several tens of degrees above the nominal AFE phase transition in samples  $x=0.04$  and  $0.1$ . This is in agreement with the coexistence of FE and AFE phases in these samples as proposed by Knudsen *et al.*,<sup>5</sup> Dai *et al.*,<sup>10</sup> and Ishchuk.<sup>13</sup> In contrast, for FE samples ( $x \leq 0.02$ ) the soft mode minimum corresponds well to  $T_C$ , and the system exhibits only a FE phase transition without any fluctuations above  $T_C$ .

A heavily damped polar soft mode with frequency near and below 1 THz was also observed in AFE  $\text{PbZrO}_3$ ,<sup>41</sup> relaxor FE PLZT 8/65/35,<sup>42</sup> and it seems to be general for all lead-based relaxors with the perovskite structure.<sup>29</sup> The soft mode is already split in the PE phase. The higher-frequency component is less damped and its frequency lies near  $60 \text{ cm}^{-1}$ .<sup>29,30,41–43</sup> It was believed, that the lower frequency component of the soft mode softens toward Burns temperature in relaxor FEs,<sup>29</sup> but very recently it was revealed in the hyper-Raman spectra of  $\text{Pb}(\text{Mg}_{1/3}\text{Nb}_{2/3})\text{O}_3$  (PMN),<sup>43</sup> that the soft mode softens to  $T^*$ , where the polar clusters become static in the relaxor phase. The most probable explanation for the soft mode splitting is the two-mode behavior due to the two-cation occupancy of the perovskite B site.

The microwave (MW) relaxations differ among the samples (see Figs. 10–12). In the FE samples ( $x=0$  and  $0.02$ ) the relaxation splits near  $T_C$  from a high-temperature excitation. Its frequency decreases on cooling and saturates near 1 GHz, where it loses its dielectric strength at low temperatures. The modulated AFE samples display somehow different behavior. In PLZT 4/90/10, at high temperatures, a broad excitation splits above  $T_C$  (probably when the local FE phase transition takes place) into two components. The lower frequency one decreases its frequency on cooling and its dielectric strength reaches a maximum at  $T_C$ . On further cooling the relaxation frequency still softens to several GHz but its dielectric strength strongly reduces.

The PLZT 10/90/10 sample shows a dielectric relaxation with frequency about 10 GHz already at 480 K, i.e., well above  $T_C$ . Its frequency is nearly temperature independent in contrast to samples with lower La concentrations. Likewise in these samples its dielectric strength shows a maximum at  $T_C$  and decreases on cooling, therefore it should be related to the nominal AFE phase transition. This relaxation probably has its origin in FE domain wall dynamics. The domain wall movement freezes at low temperatures and, therefore, its dielectric strength decreases. It could also be attributed to sound emission due to FE-ferroelastic domain wall motion.<sup>39,40</sup>

### A. Influence of La on the AFE behavior

The dielectric contributions of the different excitations are displayed in Fig. 13 together with dielectric data measured at 1 MHz. The sum of the GHz and THz contributions,  $\Sigma = \Delta\epsilon_{\text{MW}} + \Delta\epsilon_{\text{SM}}$ , fits very well the MHz permittivity. In the FE samples the contribution of the MW relaxation  $\Delta\epsilon_{\text{MW}}$  to the permittivity largely prevails, due to the presence of the FE domains. With increasing La content this relaxation weakens, because the FE domains are somehow disrupted,

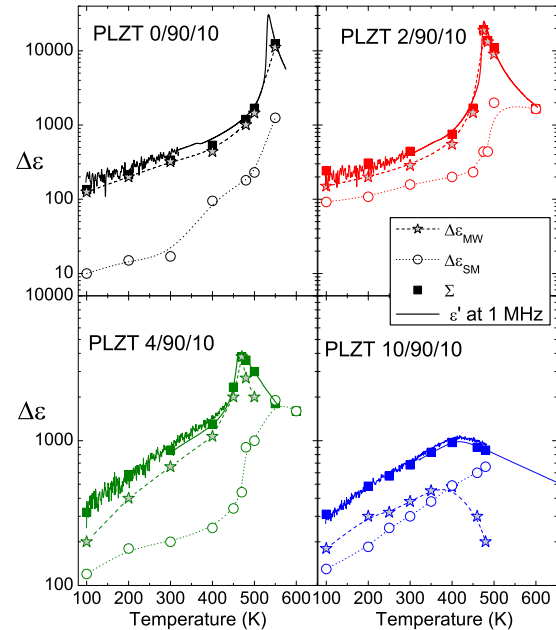


FIG. 13. (Color online) Temperature dependences of the dielectric contributions of the soft mode and GHz relaxation in PLZT  $100x/90/10$ , as well as the sum ( $\Sigma$ ) of both contributions and experimental permittivity at 1 MHz (line).

and, therefore, the permittivity value decreases significantly near  $T_C$ . The THz contribution  $\Delta\epsilon_{\text{SM}}$ , is also affected by the La doping. Its strength increases at low temperatures and also displays a pronounced temperature dependence related to the phase transitions. In comparison, the sample PLZT 10/90/10 shows very low permittivity and the  $\Delta\epsilon_{\text{MW}}$  and  $\Delta\epsilon_{\text{SM}}$  values become comparable. In simple terms, La reduces the total volume of the FE polar regions—whose switching is the principal contribution to the permittivity. This is in broad agreement with the premise that a modulated AFE phase extends within the material at the expenses of the FE phase.

The main effect of La substitution on the phonon behavior is the appearance of the intense Raman AFE soft mode near  $100 \text{ cm}^{-1}$  in PLZT 4/90/10, linked with the loss of strength of the FE soft mode near  $80 \text{ cm}^{-1}$ , as expected if the FE sample volume is reduced. The disappearance of the nonpolar Raman active localized breathing mode at  $680 \text{ cm}^{-1}$  (see Fig. 8) is probably caused by its shift to higher frequencies, together with an increase in its damping and merging with the broad band observed at  $\sim 700 \text{ cm}^{-1}$ . Additionally, La doping causes the splitting of the Raman modes at  $\sim 200 \text{ cm}^{-1}$ , E(TO2), and near  $500 \text{ cm}^{-1}$ , E(TO3) (symmetries assigned by the effective medium approximation<sup>30</sup>); see Table III. Its origin is not completely clear, although it might be related to two-mode behavior resulting from the increasing La concentration.

### V. CONCLUSIONS

Broadband dielectric spectroscopy showed that the addition of La in PZT 90/10 shifts the system from an ordered FE state to a disordered AFE state. In PLZT  $100x/90/10$  samples with  $x \geq 0.04$ , a local FE phase transition was revealed several tens of degrees above the AFE  $T_C$  from the

observed minimum of the polar soft mode frequency. The corresponding AFE soft mode was detected in the Raman spectra. These observations confirm the idea of Knudsen *et al.*,<sup>5</sup> Dai *et al.*,<sup>10</sup> and Ishchuk,<sup>11</sup> who proposed the coexistence of the FE and AFE states in these samples.

Raman spectroscopy revealed a soft mode anomaly ( $\nu \sim 80 \text{ cm}^{-1}$  at room temperature) in FE samples ( $x \leq 0.02$ ) related with a second FE phase transition. This phase transition was confirmed by dielectric measurements and is known to be due to the tilt of the oxygen octahedra, which doubles the unit cell. Therefore, this soft mode should be the antiferrodistortive soft mode of the transition in FE PLZT  $x/90/10$  samples.

Two main excitations governing the dielectric behavior were found. A THz soft mode related with the FE phase transition, and a GHz relaxation with a dominant contribution to the permittivity in the FE samples ( $x=0,0.02$ ). The FE soft mode is split into weak and strong components: at  $80 \text{ cm}^{-1}$ , and in the THz range, respectively. This behavior seems to be general for all lead-based perovskites.

## ACKNOWLEDGMENTS

This work was supported by the Academy of Sciences of the Czech Republic (Project Nos. AVOZ10100520 and KAN 301370701), by the Ministry of Industry and Trade FR-T12/165 and by the Czech Science Foundation (Project No. P204/10/0616).

<sup>1</sup>C. E. Land, P. Thatcher, and G. H. Haertling, in *Electro-Optic Ceramics*, Advances in Materials and Device Research, edited by R. Wolfe (Academic, New York, 1974), Vol. 4, pp. 137–233.

<sup>2</sup>G. H. Haertling and C. E. Land, *J. Am. Ceram. Soc.* **54**, 1 (1971).

<sup>3</sup>A. M. Glazer and S. A. Mabud, *Acta Crystallogr., Sect. B: Struct. Crystallogr. Cryst. Chem.* **B34**, 1060 (1978).

<sup>4</sup>C. Michel, J. M. Moreau, G. D. Achenbach, R. Gerson, and W. J. James, *Solid State Commun.* **7**, 865 (1969).

<sup>5</sup>J. Knudsen, D. I. Woodward, and I. M. Reaney, *J. Mater. Res.* **18**, 262 (2003).

<sup>6</sup>E. Breval, C. Wang, and J. Dougherty, *J. Am. Ceram. Soc.* **88**, 437 (2005).

<sup>7</sup>S. Teslic, T. Egami, and D. Viehland, *J. Phys. Chem. Solids* **57**, 1537 (1996).

<sup>8</sup>A. Peláiz-Barranco, J. D. S. Guerra, O. García-Zaldívar, F. Calderón-Piñar, E. B. Araújo, D. A. Hall, M. E. Mendoza, and J. A. Eiras, *J. Mater. Sci.* **43**, 6087 (2008).

<sup>9</sup>F. Jona, G. Shirane, F. Mazzi, and R. Pepinsky, *Phys. Rev.* **105**, 849 (1957).

<sup>10</sup>X. Dai, Z. Xu, J.-F. Li, and D. Viehland, *J. Mater. Res.* **11**, 626 (1996).

<sup>11</sup>D. Viehland, J.-F. Li, X. Dai, and Z. Xu, *J. Phys. Chem. Solids* **57**, 1545 (1996).

<sup>12</sup>D. Viehland, X. H. Dai, J. F. Li, and Z. Xu, *J. Appl. Phys.* **84**, 458 (1998).

<sup>13</sup>V. M. Ishchuk, V. N. Baumer, and V. L. Sobolev, *J. Phys.: Condens. Matter* **17**, L177 (2005), and references therein.

<sup>14</sup>I. MacLaren, R. Villaurrutia, and A. Peláiz-Barranco, *J. Appl. Phys.* **108**, 034109 (2010).

<sup>15</sup>D. Bäuerle and A. Pinczuk, *Solid State Commun.* **19**, 1169 (1976).

<sup>16</sup>D. Bäuerle, R. Clarke, and T. P. Martin, *Phys. Status Solidi B* **71**, K173 (1975).

<sup>17</sup>Z. Ujma, J. Handerek, M. Pawelczyk, H. Hassan, G. E. Kugel, and C. Carabatos-Nedelec, *J. Phys.: Condens. Matter* **6**, 6843 (1994).

<sup>18</sup>D. Bäuerle, W. B. Holzapfel, A. Pinczuk, and Y. Yacoby, *Phys. Status Solidi A* **83**, 99 (1977).

<sup>19</sup>J. Pokorný, J. Petzelt, I. Gregora, V. Železný, V. Vorlíček, Z. Zikmund, I. Fedorov, and M. Pronin, *Ferroelectrics* **186**, 115 (1996).

<sup>20</sup>S. Kamba, J. Petzelt, J. Banys, R. Mizaras, J. Grigas, J. Pokorny, J. Endal, A. Brilingas, G. Komandin, A. Pronin, and M. Kosec, *Ferroelectrics* **223**, 247 (1999).

<sup>21</sup>T. Ostapchuk, V. Železný, and J. Petzelt, *Proceedings of the International Conference DRP-98, Szczyrk, Poland*, edited by A. Wlochowicz (SPIE, 1999), Vol. 37DP, 151–161 (1999).

<sup>22</sup>E. Buixaderas, I. Gregora, S. Kamba, P. Kužel, and I. Reaney, *Appl. Phys. Lett.* **94**, 052903 (2009).

<sup>23</sup>J. Krupka, T. Zychowicz, V. Bovtun, and S. Veljko, *IEEE Trans. Ultrason. Ferroelectr. Freq. Control* **53**, 1883 (2006).

<sup>24</sup>P. Kužel, H. Němec, F. Kadlec, and C. Kadlec, *Opt. Express* **18**, 15338 (2010).

<sup>25</sup>A. Dreyhaupt, S. Winnerl, T. Dekorsy, and M. Helm, *Appl. Phys. Lett.* **86**, 121114 (2005).

<sup>26</sup>A. Nahata, A. S. Weling, and T. F. Heinz, *Appl. Phys. Lett.* **69**, 2321 (1996).

<sup>27</sup>P. Kužel and J. Petzelt, *Ferroelectrics* **239**, 949 (2000).

<sup>28</sup>F. Gervais, in *Infrared and Millimeter Waves*, edited by K. J. Button (Academic, New York, 1983), Vol. 8, p. 279.

<sup>29</sup>J. Hlinka, J. Petzelt, S. Kamba, D. Noujmi, and T. Ostapchuk, *Phase Transitions* **79**, 41 (2006).

<sup>30</sup>E. Buixaderas, I. Gregora, S. Kamba, J. Petzelt, and M. Kosec, *J. Phys.: Condens. Matter* **20**, 345229 (2008).

<sup>31</sup>I. Levin, E. Cockayne, M. W. Lufaso, J. C. Woicik, and J. E. Maslar, *Chem. Mater.* **18**, 854 (2006).

<sup>32</sup>S. M. Shapiro and J. D. Axe, *Phys. Rev. B* **6**, 2420 (1972).

<sup>33</sup>J. Frantti, *J. Phys. Chem. B* **112**, 6521 (2008).

<sup>34</sup>Y. Kuroiwa, Y. Terado, S. J. Kim, A. Sawada, Y. Yamamura, S. Aoyagi, E. Nishibori, M. Sakata, and M. Takata, *Jpn. J. Appl. Phys., Part 1* **44**, 7151 (2005).

<sup>35</sup>T. R. Welberry, D. J. Goossens, R. L. Withers, and K. Z. Baba-Kishi, *Metall. Mater. Trans. A* **A41**, 1110 (2010).

<sup>36</sup>W. Cochran, *Adv. Phys.* **10**, 401 (1961).

<sup>37</sup>W. Cochran and A. Zia, *Phys. Status Solidi* **25**, 273 (1968).

<sup>38</sup>G. A. Samara, *Phys. Rev. B* **1**, 3777 (1970).

<sup>39</sup>G. Arlt, U. Bottger, and S. Witte, *Ann. Phys.* **506**, 578 (1994).

<sup>40</sup>V. Porokhonsky, S. Kamba, A. Pashkin, M. Savinov, J. Petzelt, R. E. Eitel, and C. A. Randall, *Appl. Phys. Lett.* **83**, 1605 (2003).

<sup>41</sup>T. Ostapchuk, J. Petzelt, V. Zelezny, S. Kamba, and V. Bovtun, *J. Phys.: Condens. Matter* **13**, 2677 (2001).

<sup>42</sup>S. Kamba, D. Nuzhnyy, O. Tkáč, B. Malič, M. Kosec, and J. Petzelt, *Phase Transitions* **81**, 1005 (2008).

<sup>43</sup>A. Al-Zein, J. Hlinka, J. Rouquette, and B. Hehlen, *Phys. Rev. Lett.* **105**, 017601 (2010).